Array truncation effects in infrared frequency selective surfaces

Jeffrey D' Archangel,[1] Eric Tucker,[2] Markus B. Raschke,[3] and Glenn Boreman[2,*]

[1]*CREOL, The College of Optics & Photonics, University of Central Florida, 4304 Scorpius St., Orlando, FL 32816, USA*

[2]*Department of Physics and Optical Science, University of North Carolina at Charlotte, 9201 University City Blvd., Charlotte, NC 28223, USA*

[3]*Department of Physics, Department of Chemistry, and JILA, University of Colorado, 390 UCB, Boulder, CO 80309, USA*

[*]*gboreman@uncc.edu*

Abstract: A metasurface consisting of an infinite array of square loops was designed for maximal absorptivity for s-polarized light at a wavelength of 10.6 μm and 60 degrees off-normal. We investigate the effects of array truncation in finite arrays of this design using far-field FTIR spectroscopy and scattering scanning near-field optical microscopy. The far-field spectra are observed to blue-shift with decreasing array size. The near-field images show a corresponding decrease in uniformity of the local electric field amplitude and phase spatial distributions. Simulations of the far-field absorption spectra and local electric field are consistent with the measured results.

OCIS codes: (260.3910) Metal optics; (260.5740) Resonance; (310.6628) Subwavelength structures, nanostructures; (180.4243) Near-field microscopy; (300.6300) Spectroscopy, Fourier transforms; (160.3918) Metamaterials.

References and links

1. T. Maier and H. Brückl, "Wavelength-tunable microbolometers with metamaterial absorbers," Opt. Lett. **34**(19), 3012–3014 (2009).
2. A. J. Hoffman, A. Sridhar, P. X. Braun, L. Alekseyev, S. S. Howard, K. J. Franz, L. Cheng, F. Choa, D. L. Sivco, V. A. Podolskiy, E. E. Narimov, and C. Gmachl, "Midinfrared semiconductor optical metamaterials," J. Appl. Phys. **105**(12), 122411 (2009).
3. Z. H. Jiang, S. Yun, F. Toor, D. H. Werner, and T. S. Mayer, "Conformal dual-band near-perfectly absorbing mid-infrared metamaterial coating," ACS Nano **5**(6), 4641–4647 (2011).
4. J. A. Mason, S. Smith, and D. Wasserman, "Strong absorption and selective thermal emission from a midinfrared metamaterial," Appl. Phys. Lett. **98**(24), 241105 (2011).
5. S. Larouche, Y. J. Tsai, T. Tyler, N. M. Jokerst, and D. R. Smith, "Infrared metamaterial phase holograms," Nat. Mater. **11**(5), 450–454 (2012).
6. N. Yu, P. Genevet, M. A. Kats, F. Aieta, J. P. Tetienne, F. Capasso, and Z. Gaburro, "Light propagation with phase discontinuities: generalized laws of reflection and refraction," Science **334**(6054), 333–337 (2011).
7. C. L. Holloway, E. F. Kuester, J. A. Gordon, J. O'Hara, J. Booth, and D. R. Smith, "An overview of the theory and applications of metasurfaces: the two-dimensional equivalents of metamaterials," IEEE Antennas Propag. Mag. **54**(2), 10–35 (2012).
8. Q. Feng, M. Pu, C. Hu, and X. Luo, "Engineering the dispersion of metamaterial surface for broadband infrared absorption," Opt. Lett. **37**(11), 2133–2135 (2012).
9. P. E. Sieber and D. H. Werner, "Reconfigurable broadband infrared circularly polarizing reflectors based on phase changing birefringent metasurfaces," Opt. Express **21**(1), 1087–1100 (2013).
10. C. Argyropoulos, K. Q. Le, N. Mattiucci, G. D'Aguanno, and A. Alù, "Broadband absorbers and selective emitters based on plasmonic Brewster metasurfaces," Phys. Rev. B **87**(20), 205112 (2013).
11. S. Maci, G. Minatti, M. Casaletti, and M. Bosiljevac, "Metasurfing: addressing waves on impenetrable metasurfaces," IEEE Antennas Wirel. Propag. Lett. **10**, 1499–1502 (2011).
12. J. D' Archangel, E. Tucker, E. Kinzel, E. A. Muller, H. A. Bechtel, M. C. Martin, M. B. Raschke, and G. Boreman, "Near- and far-field spectroscopic imaging investigation of resonant square-loop infrared metasurfaces," Opt. Express **21**(14), 17150–17160 (2013).
13. J. Ginn, D. Shelton, P. Krenz, B. Lail, and G. Boreman, "Altering infrared metamaterial performance through metal resonance damping," J. Appl. Phys. **105**(7), 074304 (2009).

#208167 - $15.00 USD Received 12 Mar 2014; revised 18 Jun 2014; accepted 19 Jun 2014; published 27 Jun 2014

14. J. Ginn, D. Shelton, P. Krenz, B. Lail, and G. Boreman, "Polarized infrared emission using frequency selective surfaces," Opt. Express **18**(5), 4557–4563 (2010).
15. X. Liu, T. Tyler, T. Starr, A. F. Starr, N. M. Jokerst, and W. J. Padilla, "Taming the blackbody with infrared metamaterials as selective thermal emitters," Phys. Rev. Lett. **107**(4), 045901 (2011).
16. S. L. Wadsworth, P. G. Clem, E. D. Branson, and G. D. Boreman, "Broadband circularly-polarized emission from multilayer metamaterials," Opt. Mater. Express **1**(3), 466–479 (2011).
17. T. Zentgraf, J. Dorfmüller, C. Rockstuhl, C. Etrich, R. Vogelgesang, K. Kern, T. Pertsch, F. Lederer, and H. Giessen, "Amplitude- and phase-resolved optical near fields of split-ring-resonator-based metamaterials," Opt. Lett. **33**(8), 848–850 (2008).
18. P. Alonso-Gonzalez, M. Schnell, P. Sarriugarte, H. Sobhani, C. Wu, N. Arju, A. Khanikaev, F. Golmar, P. Albella, L. Arzubiaga, F. Casanova, L. E. Hueso, P. Nordlander, G. Shvets, and R. Hillenbrand, "Real-space mapping of Fano interference in plasmonic metamolecules," Nano Lett. **11**(9), 3922–3926 (2011).
19. E. C. Kinzel, J. C. Ginn, R. L. Olmon, D. J. Shelton, B. A. Lail, I. Brener, M. B. Sinclair, M. B. Raschke, and G. D. Boreman, "Phase resolved near-field mode imaging for the design of frequency-selective surfaces," Opt. Express **20**(11), 11986–11993 (2012).
20. M. Schnell, A. Garcia-Extarri, A. J. Huber, K. Crozier, J. Aizpurua, and R. Hillenbrand, "Controlling the near-field oscillations of loaded plasmonic nanoantennas," Nat. Photonics **3**(5), 287–291 (2009).
21. R. L. Olmon, M. Rang, P. M. Krenz, B. A. Lail, L. V. Saraf, G. D. Boreman, and M. B. Raschke, "Determination of electric-field, magnetic-field, and electric-current distributions of infrared optical antennas: a near-field optical vector network analyzer," Phys. Rev. Lett. **105**(16), 167403 (2010).
22. E. Tucker, J. D' Archangel, M. Raschke, E. Briones, F. J. González, and G. Boreman, "Near-field mapping of dipole nano-antenna-coupled bolometers," J. Appl. Phys. **114**(3), 033109 (2013).
23. P. M. Krenz, R. L. Olmon, B. A. Lail, M. B. Raschke, and G. D. Boreman, "Near-field measurement of infrared coplanar strip transmission line attenuation and propagation constants," Opt. Express **18**(21), 21678–21686 (2010).
24. M. Schnell, P. Alonso-Gonzalez, L. Arzubiaga, F. Casanova, L. E. Hueso, A. Chuvilin, and R. Hillenbrand, "Nanofocusing of mid-infrared energy with tapered transmission lines," Nat. Photonics **5**(5), 283–287 (2011).
25. E. Tucker, J. D' Archangel, E. Kinzel, M. B. Raschke, and G. Boreman, "Near- and far-field measurements of phase ramped structures at infrared wavelengths" (submitted).
26. J. A. D'Archangel, G. D. Boreman, D. J. Shelton, M. B. Sinclair, and I. Brener, "Releasable infrared metamaterials," J. Vac. Sci. Technol. B **29**(5), 051806 (2011).
27. W. L. Chan, H. Chen, A. J. Taylor, I. Brener, M. J. Cich, and D. M. Mittleman, "A spatial light modulator for terahertz beams," Appl. Phys. Lett. **94**(21), 213511 (2009).
28. F. Alves, D. Grbovic, B. Kearney, and G. Karunasiri, "Microelectromechanical systems bimaterial terahertz sensor with integrated metamaterial absorber," Opt. Lett. **37**(11), 1886–1888 (2012).
29. F. Alves, D. Grbovic, B. Kearney, N. V. Lavrik, and G. Karunasiri, "Bi-material terahertz sensors using metamaterial structures," Opt. Express **21**(11), 13256–13271 (2013).
30. A. M. M. A. Allam and E. A. Parker, "Application of Pocklington's equation to analysis of dipole frequency-selective surfaces of finite size," IEEE Proc.-H **134**, 521–526 (1987).
31. R. Kastner and R. Mittra, "Iterative analysis of finite-sized planar frequency selective surfaces with rectangular patches of perforations," IEEE Trans. Antenn. Propag. **35**(4), 372–377 (1987).
32. W. L. Ko and R. Mittra, "Scattering by a truncated periodic array," IEEE Trans. Antenn. Propag. **36**(4), 496–503 (1988).
33. C. Pochini, G. Toso, G. Pelosi, and A. Roederer, "A comparison between two hybrid techniques for the scattering from finite frequency-selective surfaces," Microw. Opt. Technol. Lett. **31**(4), 248–252 (2001).
34. V. V. S. Prakash and R. Mittra, "Convergence studies of plane-wave spectral expansion technique for analyzing truncated frequency-selective surfaces," Microw. Opt. Technol. Lett. **34**(6), 417–421 (2002).
35. F. Capolino and M. Albani, "Truncation effects in a semi-infinite periodic array of thin strips: a discrete Wiener-Hopf formulation," Radio Sci. **34**, RS2S91 (2009).
36. B. A. Munk, D. S. Janning, J. B. Pryor, and R. J. Marhefka, "Scattering from surface waves on finite FSS," IEEE Trans. Antenn. Propag. **49**(12), 1782–1793 (2001).
37. D. S. Janning and B. A. Munk, "Effects of surface waves on the currents of truncated periodic arrays," IEEE Trans. Antenn. Propag. **50**(9), 1254–1265 (2002).
38. M. Lapine, L. Jelinek, M. J. Freire, and R. Marqués, "Realistic metamaterial lenses: limitations imposed by discrete structure," Phys. Rev. B **82**(16), 165124 (2010).
39. W. Withayachumnakul, C. Fumeaux, and D. Abbott, "Planar array of electric-LC resonators with broadband tenability," IEEE Antennas Wirel. Propag. Lett. **10**, 577–580 (2011).
40. G. I. Kiani, L. G. Olsson, A. Karlsson, K. P. Esselle, and M. Nilsson, "Cross-dipole bandpass frequency selective surface for enerfy-saving glass used in buildings," IEEE Trans. Antenn. Propag. **59**(2), 520–525 (2011).
41. M. Lapine, L. Jelinek, and R. Marqués, "Surface mesoscopic effects in finite metamaterials," Opt. Express **20**(16), 18297–18302 (2012).
42. L. W. Cross, M. J. Almalkawi, and V. K. Devabhaktuni, "Development of large-area switchable plasma device for X-band applications," IEEE Trans. Plasma Sci. **41**(4), 948–954 (2013).

#208167 - $15.00 USD Received 12 Mar 2014; revised 18 Jun 2014; accepted 19 Jun 2014; published 27 Jun 2014

43. P. W. Grounds and K. J. Webb, "Numerical analysis of finite frequency selective surfaces," in *Antennas and Propagation Society International Symposium* (APS Digest, 1988), pp. 746–749.
44. S. B. Savia, E. A. Parker, and B. Phillips, "Finite planar- and curved-ring-element frequency-selective surfaces," IEEE Proc. Microw. Antennas Propag. **146**(6), 401–406 (1999).
45. E. A. Parker, J. B. Robertson, B. Sanz-Izquierdo, and J. C. Batchelor, "Minimal size FSS for long wavelength operation," Electron. Lett. **44**(6), 394 (2008).
46. C. Guclu, J. Sloan, S. Pan, and F. Capolino, "High impedance surface as an antenna without a dipole on top," in *2011 IEEE International Symposium on Antennas and Propagation*, pp. 1028–1031.
47. E. Irci, K. Sertel, and J. Volakis, "An extremely low profile, compact, and broadband tightly coupled patch array," Radio Sci. **47**(3), RS0M06 (2012).
48. I. T. Ekpo, J. C. Batchelor, and E. A. Parker, "Transmitted power distribution across a minimal size FSS for long wavelength operation," in *2010 Loughborough Antennas and Propagation Conference*, pp. 553–556.
49. J. Bravo-Abad, A. Degiron, F. Przybilla, C. Genet, F. J. García-Vidal, L. Martín-Moreno, and T. W. Ebbesen, "How light emerges from an illuminated array of subwavelength holes," Nat. Phys. **2**(2), 120–123 (2006).
50. V. A. Fedotov, N. Papasimakis, E. Plum, A. Bitzer, M. Walther, P. Kuo, D. P. Tsai, and N. I. Zheludev, "Spectral collapse in ensembles of metamolecules," Phys. Rev. Lett. **104**(22), 223901 (2010).
51. K. Bao, N. A. Mirin, and P. Nordlander, "Fano resonances in planar silver nanosphere clusters," Appl. Phys. A. Mater. Sci. **100**(2), 333–339 (2010).
52. J. B. Lassiter, H. Sobhani, M. W. Knight, W. S. Mielczarek, P. Nordlander, and N. J. Halas, "Designing and deconstructing the Fano lineshape in plasmonic nanoclusters," Nano Lett. **12**(2), 1058–1062 (2012).
53. J. Ye, F. Wen, H. Sobhani, J. B. Lassiter, P. Van Dorpe, P. Nordlander, and N. J. Halas, "Plasmonic nanoclusters: near field properties of the Fano resonance interrogated with SERS," Nano Lett. **12**(3), 1660–1667 (2012).
54. S. A. Maier, P. G. Kik, and H. A. Atwater, "Optical pulse propagation in metal nanoparticle chain waveguides," Phys. Rev. B **67**(20), 205402 (2003).
55. B. Willingham and S. Link, "Energy transport in metal nanoparticle chains via sub-radiant plasmon modes," Opt. Express **19**(7), 6450–6461 (2011).
56. S. A. Maier, P. G. Kik, and H. A. Atwater, "Observation of coupled plasmon-polariton modes in Au nanoparticle chain waveguides of different lengths: estimation of waveguide loss," Appl. Phys. Lett. **81**(9), 1714–1716 (2002).
57. I. Horcas, R. Fernández, J. M. Gómez-Rodríguez, J. Colchero, J. Gómez-Herrero, and A. M. Baro, "WSXM: a software for scanning probe microscopy and a tool for nanotechnology," Rev. Sci. Instrum. **78**(1), 013705 (2007).
58. M. L. M. Balistreri, J. P. Korterik, L. Kuipers, and N. F. van Hulst, "Local observations of phase singularities in optical fields in waveguide structures," Phys. Rev. Lett. **85**(2), 294–297 (2000).
59. M. L. M. Balistreri, J. P. Korterik, L. Kuipers, and N. F. van Hulst, "Phase mapping of optical fields in intergrated optical waveguide structures," J. Lightwave Technol. **19**(8), 1169–1176 (2001).
60. J. N. Walford, K. A. Nugent, A. Roberts, and R. E. Scholten, "High-resolution phase imaging of phase singularities in the focal region of a lens," Opt. Lett. **27**(5), 345–347 (2002).
61. U. Kreibig and M. Vollmer, *Optical Properties of Metal Clusters* (Springer, 1995).

1. Introduction

Optical metamaterials are an engineered class of materials which exhibit properties not typically found in nature. Several recent efforts have focused attention on the control of spectral properties [1–4] and phase [5, 6] at infrared wavelengths. The term *metasurface* has been introduced as a description for metamaterials consisting of planar periodic arrays of scatterers or apertures which form a surface much thinner than the design wavelength [7–12]. In many cases, the desired performance is obtained by employing metamaterial designs inspired by frequency selective surfaces (FSS) whose functionality was shown long ago for radio communications [13–16].

Metasurfaces and other sub-wavelength periodic structures are almost universally simulated as infinite arrays along the directions of periodicity, by considering a single unit cell with the appropriate boundary conditions. This greatly reduces the computational effort for simulation and is a good approximation for most applications. However, all metasurfaces and related structures are necessarily finite. The actual size limit of the arrays is enforced by various circumstances which can be application specific, related to the cost of fabrication, or ultimately limited to the size which can be realistically manufactured. In addition, the interaction of a beam of light of finite size can cause an equivalent form of array truncation if the number of illuminated elements is small compared to the number necessary for the desired optical property to converge to that of an infinite array. It is clear that below some threshold

#208167 - $15.00 USD Received 12 Mar 2014; revised 18 Jun 2014; accepted 19 Jun 2014; published 27 Jun 2014

the finite size of truncated arrays will significantly alter the device performance in terms of the near- and far-field response.

Here, we report on the design, fabrication, and characterization of a square loop mid-infrared (mid-IR) metasurface which has been created to demonstrate the effects of array truncation in the near- and far-field. The far-field measurements were carried out using an FTIR based ellipsometer in reflectivity mode, while the near-field measurements were made using scattering-scanning near-field optical microscopy (*s*-SNOM). Measurements of local electric field distributions using *s*-SNOM at mid-IR wavelengths have been shown recently for metamaterial samples [12, 17–19], as well as antennas [20–22], transmission lines [23, 24], and phase-ramped structures [25]. The data presented in this report show the effects of truncation on the near- and far-field performance of a mid-IR metasurface by comparing the infinite array response with that of 11x11 arrays, 7x7 arrays, 3x3 arrays, and single square loops with a large periodicity.

The investigation into array truncation was inspired by a previous effort where infinite metasurface arrays were etched into small square flakes toward the creation of a large area, conformal metasurface coating [26]. Here, the reflectivity spectra of the truncated arrays compared somewhat favorably with that of the infinite arrays, but the extent to which array truncation altered the spectra was unclear [26]. Aside from this particular application, our results are relevant for the design of metamaterial enhancement of pixel-scale sensors [1, 27–29], as well as all other areas where truncated metamaterial arrays are employed. The results and discussion should serve as a baseline study for the effects of array truncation on optical metasurfaces and related structures.

Truncation effects in FSS and metamaterial structures in the radio frequency (RF) band have been studied, with much of the work being concerned with the development of hybrid simulation techniques [30–35] as well as the presence of surface waves on finite arrays [36, 37]. In addition there are several examples at RF where the effects of finite arrays are addressed in the discussion of the deviation between the performance of the fabricated or realistic sample and theory [38–42]. The most relevant literature at RF is that which relates to resonant spectral shifts due to truncation [43–47] as well as one reference which shows near-field measurements on a 3x3 truncated array [48]. However, to the best of our knowledge, there are no examples in the literature on the study of truncation effects in metasurfaces or related structures at mid-IR frequencies.

There are a few examples at visible wavelengths which investigate finite structures which are similar to metasurfaces. The angular dependence of throughput with respect to number of aperture elements has been investigated for extraordinary optical transmission applications [49]. In another example, the transmission through finite asymmetric metamaterial arrays was reported as a step toward a lasing spaser [50]. Additionally, spectral shifting of the Fano resonance has been noted in plasmonic nanoclusters with varying number of nanoparticles [51–53]. Perhaps the most relevant prior work at optical frequencies concerns plasmon waveguides, where a splitting between the resonance wavelength of the longitudinal and transverse modes was simulated [54, 55] and observed experimentally [54, 56] for finite one dimensional arrays of plasmonic elements.

2. Sample design and fabrication

For the purposes of investigating truncation effects both in the near- and the far-field, a sample was designed with optimized absorptivity at 10.6 μm at an angle 60 degrees from normal incidence. This wavelength and angle of incidence correspond to the typical excitation scheme of the *s*-SNOM apparatus in the near-field. The design consisted of Au square loops above a ZnS standoff layer and Cr ground plane. ZnS was chosen due to its transparency at mid-IR wavelengths, while Cr was chosen as a ground plane material due to good adhesion to ZnS and Si. The design was then simulated by Floquet analysis at 60 degrees off-normal in Ansys HFSS using optical properties derived from ellipsometry; the metasurface was

#208167 - $15.00 USD Received 12 Mar 2014; revised 18 Jun 2014; accepted 19 Jun 2014; published 27 Jun 2014

optimized for absorptivity via iterative tuning of the thickness of the ZnS layer, the square loop dimensions, and the periodicity. The dimensions of the optimized design are as follows: the ZnS thickness was 320 nm, the square loop edge length was 1.44 μm, and the periodicity was 1.79 μm.

Fabrication of the structures was performed using electron beam lithography and lift-off. First, a 150 nm Cr ground plane was deposited on to a clean 4" Si wafer via electron beam evaporation. The ZnS layer was deposited by thermal evaporation using a baffled box to enhance film uniformity. The square loops were patterned via electron beam lithography with a JEOL JBX-9300FS system, using PMMA as resist. The exposed areas were developed in a solution of equal parts methyl isobutyl ketone (MIBK) and isopropyl alcohol (IPA) for 2 minutes. Metallization was carried out by electron beam evaporation of a 2.5 nm adhesion layer of Ti followed by a 75 nm layer of Au. Liftoff was achieved by submerging the sample in n-methyl pyrrolidinone (NMP) for approximately 24 hours.

Six patterned areas 3 mm x 8 mm in size were fabricated on the sample. These patterned areas consisted of the non-truncated design (henceforth called the "infinite array") as well as truncated arrays of the original design containing 11x11, 7x7, 5x5, and 3x3 square loop elements as well as isolated square loop elements. In the case of the isolated loops and truncated loop arrays, the adjacent space between the structures was 6.35 μm. This was observed in the initial simulations to be a distance where the arrays had enough fill factor to provide significant absorptivity for the far-field measurement along with a lack of significant near-field interaction between adjacent arrays. It is noted that the variation in pattern density between the six patterned areas initially caused fabrication inconsistencies between the different sized arrays due to proximity effects in the lithographic exposure. To ensure that the geometry of the elements in the truncated arrays remained true to the original design, the electron beam doses were varied and the pattern line widths were biased over several dose matrices until the correct dimensions were observed for each patterned area by high resolution scanning electron microscopy (SEM). SEM images representing each patterned area of the fabricated sample are shown in Fig. 1.

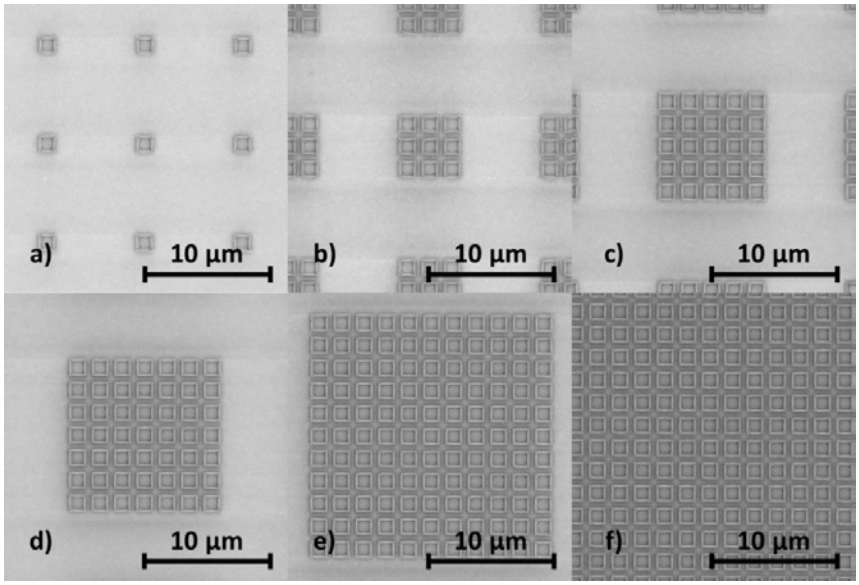

Fig. 1. SEM images depicting square loop arrays of increasing size: a) isolated square loops, b) 3x3 element arrays, c) 5x5 arrays, d) a 7x7 array, e) an 11x11 array, and f) the infinite array of the original design.

#208167 - $15.00 USD Received 12 Mar 2014; revised 18 Jun 2014; accepted 19 Jun 2014; published 27 Jun 2014

3. Characterization methods

3.1 Far-field characterization

The spectral absorptivity was measured at 60 degrees off-normal using an infrared variable-angle spectroscopic ellipsometer (IR-VASE, J. A. Woollam). The ellipsometer was run in reflectivity mode with the source and detector filters configured for s-polarization. Since the sample has an optically thick ground plane, the absorptivity A is simply calculated from the reflectivity R as $A = 1 - R$.

While the measurement of reflectivity at 60 degrees off-normal was easily performed using the ellipsometer, issues arose due the discrepancy between the size of the IR beam and the size of the patterned areas on the sample. The interrogation area on the sample at 60 degrees is approximately 1 cm x 2 cm, much larger than the area of interest. Additionally, the light impinging upon the sample area is not a uniform beam, but rather a slightly focused image of the infrared glow-bar source, with a "U" shaped intensity profile. Since the beam is not uniform, the aperture at the source cannot be simply made smaller to accommodate the small sample size. To mitigate these issues, custom masks were fabricated with rectangular apertures centered about the brightest observed intensity from the glow-bar at the sample area. Several aperture sizes were tested, but during the reflectivity measurements it was observed that the smallest aperture to yield a suitable signal to noise ratio was 4 mm x 10 mm. The measurement area thus contained all of the sample area of 3 mm x 8 mm along with additional sample area outside of the patterned area, consisting of bare ZnS on Cr. The latter led to an overall lower measured absorptivity, as will be discussed later.

3.2 Near-field characterization

The local infrared near-field polarized normal to the square loops (p-polarization with respect to the sample) was measured by a custom built *s*-SNOM system [19]. A schematic of the apparatus is shown in Fig. 2. The source is a CO_2 laser, tuned to 10.25 μm. The incident beam is expanded and collimated with s-polarization with respect to the sample. The apparatus is arranged in a Michelson configuration, with a beam splitter allowing for part of the incident wave front to be transmitted to the sample area while the remaining wave front is reflected into the reference arm. The transmitted beam is directed toward the sample by planar mirrors and focused onto the sample area with an off-axis parabolic reflector (OAP).

The beam at the sample is s-polarized with an elliptical waist of approximately 65 μm spatial extent along the short axis in the sample plane. However, even for the largest sample area measured of 22 μm^2 the excitation field is still well-approximated as a plane wave. Additionally, for the s-SNOM measurements the sample is scanned underneath the stationary beam focus, so the measurement area on the sample is consistently being excited with the uniform amplitude and phase front at the center of the Gaussian focus. A Pt-coated AFM probe operating in tapping mode is positioned at the focus of the beam, which allows the local resonant evanescent fields on the sample to be scattered back into the system and detector.

The reference arm consists of a moveable mirror that is used to adjust the path length of the reference beam as well as a quarter wave plate to attenuate the polarization state of interest. The reference and sample beams are recombined at the beam splitter and passed through a wire grid polarizer, which allows p-polarization (with respect to the sample) to pass through, corresponding to the near-field signal polarized normal to the square loops on the sample. For the results shown here, the square loop structures are excited using s-polarization and the p-polarized light in the near-field is measured.

#208167 - $15.00 USD Received 12 Mar 2014; revised 18 Jun 2014; accepted 19 Jun 2014; published 27 Jun 2014

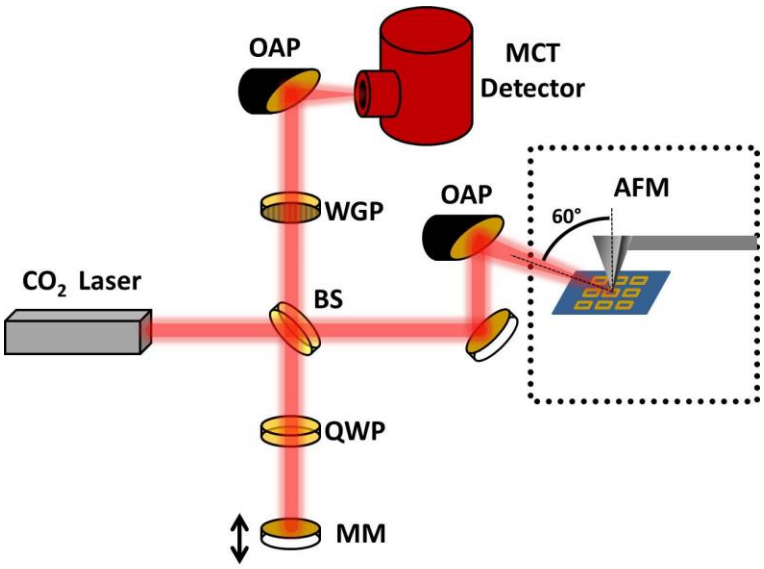

Fig. 2. Schematic of the s-SNOM apparatus.

The interfering beams are sampled with a HgCdTe (MCT) detector, using a lock-in amplifier to sample the signal at the second-harmonic of the AFM tip dither frequency. The intensity at the detector can be expressed as follows [19, 22, 25].

$$I_d \propto \left|E_{scat} + E_{ref}\right|^2 = \left|E_{scat}\right|^2 + \left|E_{ref}\right|^2 + 2\left|E_{scat} \cdot E_{ref}\right| \cos\varphi + I_b \qquad (1)$$

Here E_{scat} is the field of the scattered sample beam, E_{ref} is the field of the reference beam, φ is the phase difference between the two beams, and I_b represents a background signal which is not related to either the sample signal or reference beam. The terms which do not oscillate according to φ are diminished significantly due to the use of the lock-in amplifier as well as the orthogonally polarized excitation and detection scheme [17, 19, 20, 22, 23, 25]. In order to generate amplitude and phase images, several data sets are taken over the sample area of interest at different discrete reference phases. The results are exported as text files via WSxM [57]. The scans are then processed, point by point, using a least squares fit to a cosine function with respect to the reference phase. The output is a set of spatial maps over the sample area of interest with each point taking the following form.

$$S\left(\varphi_{rel}\right) = S_0 + S_A \cos\varphi_{rel} \qquad (2)$$

Here, S_0 is an offset term that does not vary with φ_{rel}, S_A is an amplitude term that is proportional to the amplitude of the local electric field, and φ_{rel} is an arbitrary relative phase value. It is noted that for all possible relative phase values, the point-by-point spatial relationship in phase on the sample will be maintained.

4. Results

4.1 Far-field FTIR

The spectral absorptivity (using s-polarized light) of the patterned structures at 60 degrees off-normal was measured using the infrared ellipsometer apparatus as described previously. While the infinite array simulations were performed using Floquet port analysis, the finite array simulations were performed using plane wave excitation with s-polarization at 60 degrees off normal. Absorptivity was calculated in the Floquet analysis by way of the

#208167 - $15.00 USD Received 12 Mar 2014; revised 18 Jun 2014; accepted 19 Jun 2014; published 27 Jun 2014

scattering parameters, while the finite array simulations obtained absorptivity by integrating the volume loss density over the simulated volume and then normalizing the results to the excitation intensity. The measured and simulated spectra are shown in Fig. 3. As can be seen, the wavelength of peak experimental absorptivity shifts from approximately 10.25 μm for the infinite array to approximately 9.35 μm for the single isolated loops. The underlying causes for the shift in peak resonance are discussed thoroughly in the following section. The decrease in the amplitude of absorptivity with decreasing array size is predominantly due to the decreased fill factor of elements within the measurement area. The simulated spectra show the same general trend, although the simulations show more abrupt changes in the resonant wavelength.

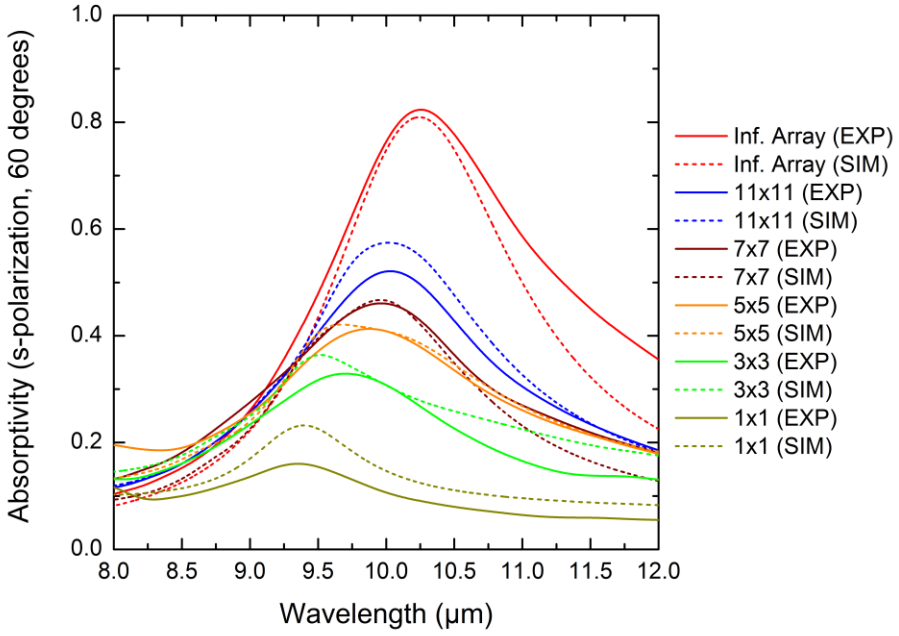

Fig. 3. Measured and simulated spectral absorptivity for the infinite array and truncated arrays, at 60 degrees off-normal for s-polarization.

The wavelength of resonance for the infinite array is found to be near 10.25 μm when it was stated previously that the sample was designed for peak absorptivity at 10.6 μm, 60 degrees angle of incidence. Upon investigation via SEM it was found that the fabricated structures were actually slightly smaller than intended (the edge length of the loops was ~50 nm shorter than the specified design). Additionally, the corners were slightly rounded compared to the idealized simulation. As the resonant wavelength of a square loop is related directly to the perimeter, this slight difference in geometry shortened the wavelength of resonance correspondingly. Therefore, the simulated values shown in Fig. 3 have been adjusted to show this difference by re-simulating the actual dimensions with a loop edge length of 1.39 μm.

The infinite array is observed to be ~80% absorptive at the resonant wavelength, whereas the design was optimized to approach unity absorptivity at resonance. The weaker than expected measured absorptivity can be attributed to the additional un-patterned areas within the aperture mask which defined the area that was actually measured. Indeed, the sample area of interest was much more absorptive than implied by Fig. 3; however, the measured sample

#208167 - $15.00 USD Received 12 Mar 2014; revised 18 Jun 2014; accepted 19 Jun 2014; published 27 Jun 2014

area included regions around the arrays void of square loops. The percentage of this area is calculated geometrically to be approximately 20% (considering the finite thickness of the mask and absorptive mask coating). The simulated values shown in Fig. 3 take into account the mixture of the arrays and the perimeter voids as follows.

$$A(\lambda)_{Total} = FF \cdot A(\lambda)_{S.L.} + (1 - FF) \cdot A(\lambda)_{Substrate} \quad (3)$$

Here, *FF* is the proportion of the arrays filling the masked aperture, termed the *fill-factor*, $A(\lambda)_{S.L.}$ is the simulated absorptivity of the arrays, and $A(\lambda)_{Substrate}$ is the simulated absorptivity of the un-patterned substrate. The absorptivity of the infinite array was also measured at normal incidence using FTIR with a microscope attachment to measure a 100 μm diameter circular sample area filled with loop elements. This measurement (data not shown) concluded that indeed the absorptivity of the original design has a maximum value of 0.98 near 10.6 μm.

To highlight the spectral shifts in Fig. 3 due to truncation, Fig. 4 depicts the peak wavelengths (a) and corresponding FWHM (b). This shows the gradual shift of the wavelengths of maximum resonance for the truncated arrays from that of the infinite array value for both the experiment and the simulations. The deviations between theory and experiment for the 3x3 and 5x5 arrays are likely due to interference effects that are sometimes seen in the modeling when the lateral dimensions of the array are close to the wavelengths of interest. These simulated effects come about due to the perfect coherence assumed in the simulations, whereas the experiment uses a broadband incoherent source and does not experience these effects. The experimental and simulated FWHM values of the absorptivity peaks fluctuate somewhat through the truncated values, as might be expected due to the changes in resonance. For every array measured, the experimental bandwidth is larger than the simulated bandwidth, which can presumably be attributed to structural inhomogeneities in the fabricated compared to the ideal geometry.

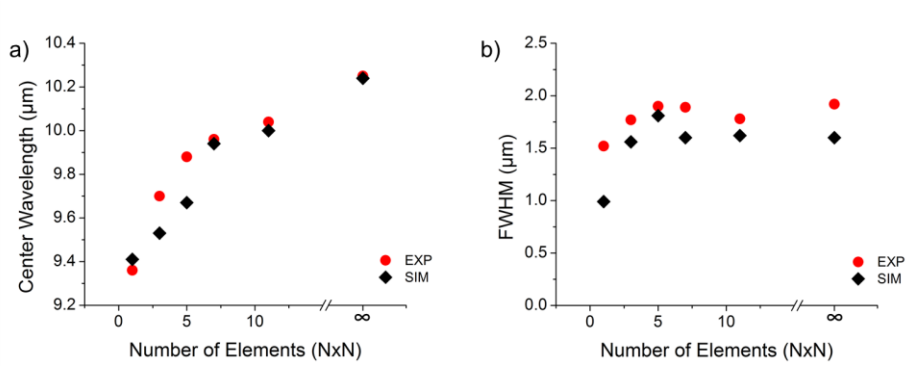

Fig. 4. Peak wavelength (a) and FWHM (b) derived from measured and simulated absorptivity spectra shown in Fig. 3.

4.2 Near-field imaging

s-SNOM images are acquired at an excitation wavelength of 10.25 μm corresponding to the peak wavelength of the largest array, and still well within the observed experimental bandwidth of the fabricated arrays (with the exception of the isolated loops). Figure 5 shows the measured and simulated amplitude of the local electric field signal polarized in the direction normal to the square loops (p-polarized with respect to the sample) for an area of the infinite array (a,d), an 11x11 array (b,e), and a 7x7 array (c,f). The experimental results were obtained by sampling 256 x 256 data points on square sample areas 22 μm per side, corresponding to an area slightly larger than the 11x11 arrays. As can be seen for the infinite array, the experimental and simulated results show a high degree of uniformity, with each

#208167 - $15.00 USD Received 12 Mar 2014; revised 18 Jun 2014; accepted 19 Jun 2014; published 27 Jun 2014

element exhibiting the expected symmetric dipolar amplitude pattern with a minima at the center of each horizontal edge.

The effects of truncation can be seen for the finite arrays as disruptions in the amplitude uniformity, with the dipolar pattern for most of the elements becoming asymmetric in terms of the amplitude on each vertical edge of the loops as well as the position of the horizontal minima. Insets of the center three elements for each array in Fig. 5 are included to illustrate more clearly the differences in field amplitude between the infinite and truncated arrays. It can be seen noticeably for the truncated arrays that only the center column of elements shows a local electric field distribution which is similar to the dipolar pattern observed in the unit cells of the infinite array. As expected, the simulated and experimental amplitude values show the effects of truncation more strongly in the horizontal direction due to inter-element coupling along the direction of the excitation polarization (s-polarized, horizontal in the Figs.) and much less coupling along the vertical direction.

While the simulations do not replicate all experimental near-field details of the truncated arrays, there is good overall qualitative agreement. For example, there is strong experimental amplitude observed at the top, center region of the 11x11 array (dotted circle) which is clearly predicted in the simulation. Additionally, simulation and experiment share the amplitude variations from row to row for the 7x7 array. Moreover, the pattern of the experimental amplitude distribution from column to column is well reproduced by the simulations for most of the columns in both truncated arrays shown in Fig. 5.

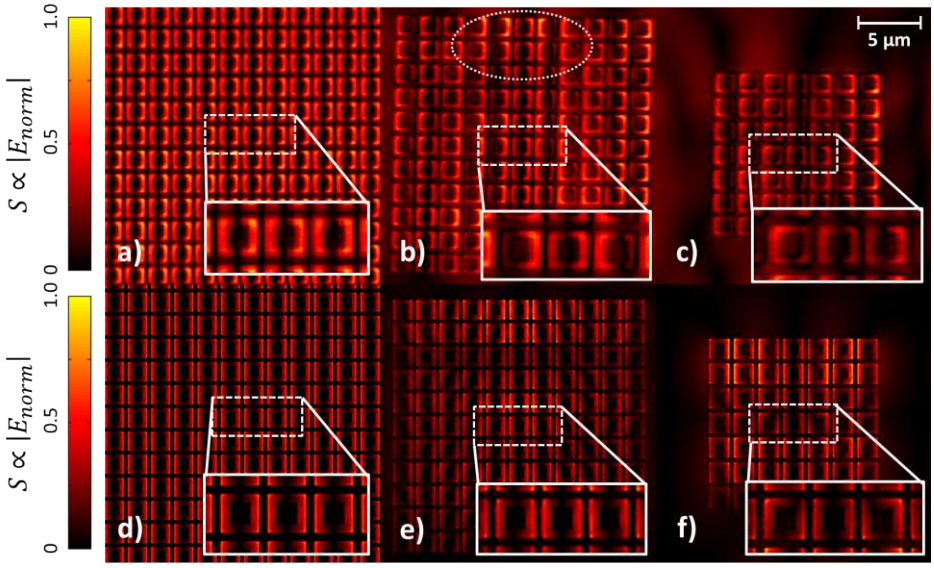

Fig. 5. Measured near-field amplitude images for polarization normal to the loops (p-polarization) for a) the infinite array, b) an 11x11 array, and c) a 7x7 array, and corresponding simulated near-field amplitude values for d) the infinite array, e) an 11x11 array, and f) a 7x7 array.

Figure 6 depicts the measured and simulated amplitude of the electric field polarized in the direction normal to the sample for the next smaller arrays of 5x5, 3x3, and the single loops. The experimental results were again obtained by sampling 256 x 256 data points as before; however, to obtain better resolution the square sample area in this case was 11 µm per side, corresponding to an area slightly larger than the 5x5 array size. Similar truncation effects can be seen experimentally in the 5x5 and 3x3 arrays as was seen in the previous Fig. for the 11x11 and 7x7 arrays. It is observed again that in the truncated results the center column of elements shows the symmetric dipolar pattern which is expected for resonant

#208167 - $15.00 USD Received 12 Mar 2014; revised 18 Jun 2014; accepted 19 Jun 2014; published 27 Jun 2014

square loops. As before, there is a good qualitative match between the experiment and simulations. For the 5x5 array, the strong experimental field amplitude in the second row is predicted well by the simulations. However, the experimental amplitude variations from column to column differ from the simulated values. As expected, the local electric field distribution appears roughly symmetric from left to right in the horizontal direction for the 5x5 and 3x3 arrays, although the right edge of the 3x3 array appears brighter than the left.

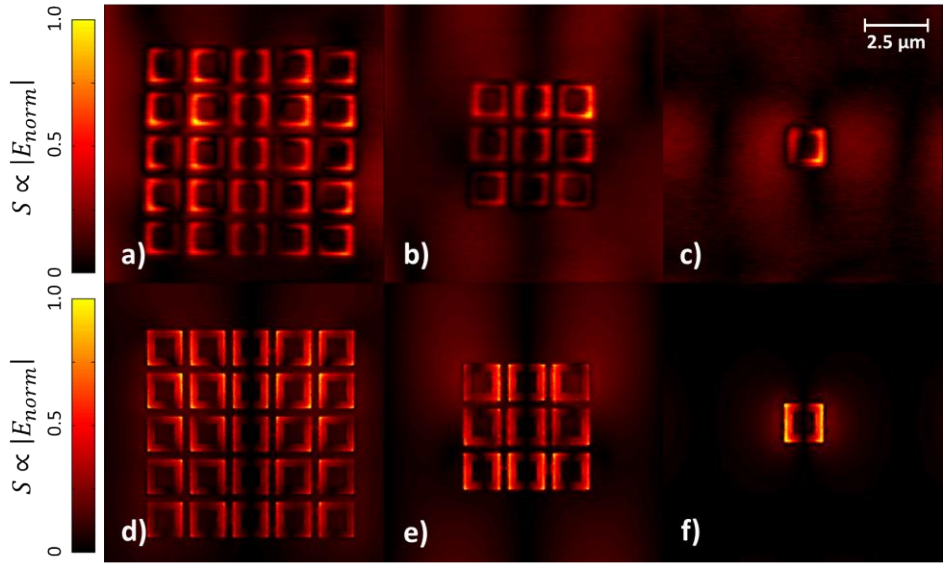

Fig. 6. Measured near-field amplitude images for polarization normal to the loops (p-polarization) for a) a 5x5 array, b) a 3x3 array, and c) an isolated square loop, and corresponding simulated near-field amplitude values for d) a 5x5 array, e) a 3x3 array, and f) an isolated loop.

The most notable difference between the experimental and simulated images is seen in the elements at the left and right edges of the arrays, which are observed to have strong field amplitude in the experiment and appear weaker in the simulation. However, the near-field simulations of the finite arrays were performed with master and slave boundaries to enforce the correct periodicity and thus are presumed to correctly interpret the coupling between adjacent arrays. As was observed in the previous Fig. for the larger finite arrays, the effects of truncation on the near-field experimental amplitude seem more significant than what is predicted by the simulations. The 3x3 array and isolated loop show an asymmetric experimental amplitude pattern that is not found in the simulations and contrary to basic expectation. We believe that the asymmetry observed experimentally for the 3x3 arrays and single loops is due to a far-field interference background, which is more pronounced as the resonant amplitude is reduced and less noticeable in structures which are highly resonant. It is noted that the asymmetry and background amplitude seen in Fig. 6 was not reduced by incremental alignments of the apparatus. It is additionally noted that the inhomogeneities and curved edges of the fabricated geometry may also have some effect of the differences observed between theory and experiment in the near field.

The effects of array truncation are also observed when plotting the cosine of the relative phase of the local electric field; phase images corresponding to Fig. 5 are shown in Fig. 7, where the cosine of the phase is shown rather than the raw relative phase to highlight the phase relationships and dilute the graphical anomalies caused by phase wrapping between $-\pi$ and π [58–60]. The phase images show uniformity in the infinite array, while the phase of the 11x11 and 7x7 truncated arrays appears to show a collective oscillation. The phase images

#208167 - $15.00 USD Received 12 Mar 2014; revised 18 Jun 2014; accepted 19 Jun 2014; published 27 Jun 2014

corresponding to Fig. 6 are shown in Fig. 8. As was observed in the larger truncated arrays, the 5x5 and 3x3 arrays show non-uniformity across the truncated arrays and a collective oscillation in the phase images.

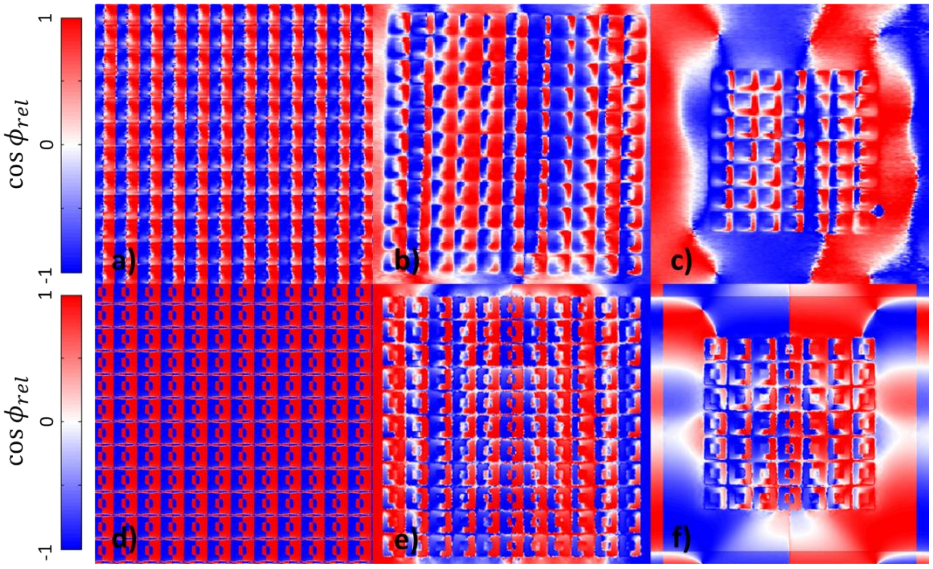

Fig. 7. Cosine of the relative phase for polarization normal to the loops (p-polarization) as measured for a) the infinite array, b) an 11x11 array, and c) a 7x7 array, as well as corresponding simulated values for d) the infinite array, e) an 11x11 array, and f) a 7x7 array. The results were obtained with a 22 μm square sample area.

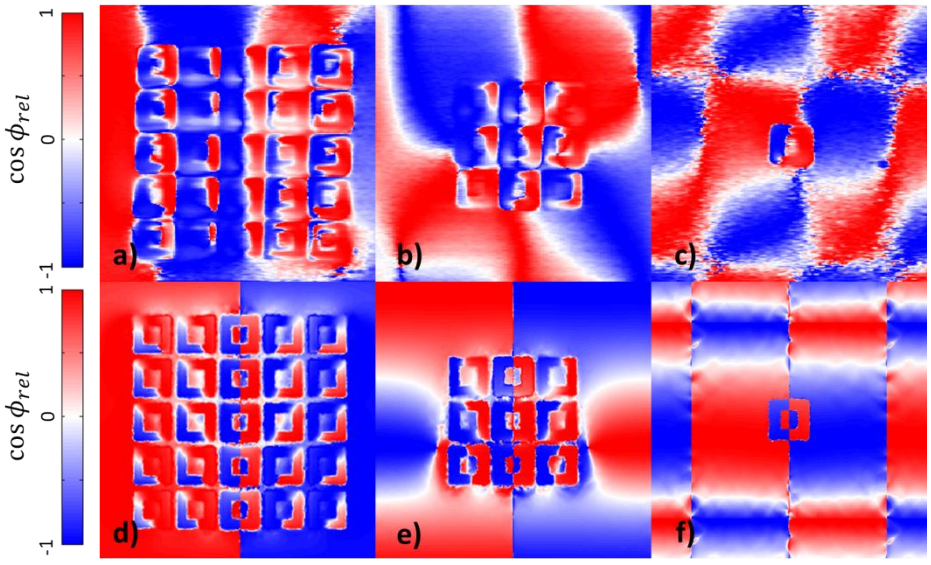

Fig. 8. Cosine of the relative phase for polarization normal to the loops (p-polarization) as measured for a) a 5x5 array, b) a 3x3 array, and c) an isolated square loop, as well as corresponding simulated values for d) a 5x5 array, e) a 3x3 array, and f) an isolated loop. The results were obtained with a 11 μm square sample area.

#208167 - $15.00 USD Received 12 Mar 2014; revised 18 Jun 2014; accepted 19 Jun 2014; published 27 Jun 2014

5. Discussion

While the changes in near-field distribution between the different array sizes may seem small, they underlie the significant spectral shift of the corresponding far-field resonance spectral position. Such spectral shift has been noted previously at RF. For example, Grounds and Webb showed through simulations that the resonant wavelength of a patch array FSS which was infinite in one dimension and 3 elements wide in the other is slightly shorter than that of the doubly periodic array at both normal and 30 degree angles of incidence [43]. Guclu et al., also at RF, showed via simulation that the peak in gain of finite high impedance surfaces occurs at shorter wavelengths as the number of elements in the array is reduced [46]. Kiani et al. measured transmission through a 2x2 cross-dipole FSS at RF, and the data showed that the peak transmission occurred at a slightly shorter wavelength as opposed to the infinite array theoretical prediction [40]. Savia, Parker, and Philips showed simulated results for circular ring arrays on a triangular lattice that indicate a shifting of resonance toward shorter (radio) wavelengths upon truncation from an infinite to a 91 element array [44].

There are several examples of similar behavior in patterned structures at optical frequencies. Fedetov et al. experimentally showed a slight shifting of the resonant transmission dip associated with a trapped-mode resonance for finite arrays of asymmetric metamaterials at near-infrared wavelengths [50]. Bao, Mirin, and Nordlander observed a red-shifting in the Fano resonance with respect to the number of nanoparticles ranging from one to seven [51]. Red-shifting of the Fano resonance was similarly noted for nanoclusters where the center element grew in size to accommodate a larger number of perimeter nanoparticles [51–53]. Additionally, Maier, Kik, and Atwater showed that the longitudinal mode plasmon resonance energies of nanoparticle chains were shifted higher as the number of nanoparticles was reduced in both simulations [54, 56] and an experimental study [56]. This behavior was again seen in simulated nanoparticle chains by Willingham and Link [55]. Overall, examples in the prior work tend to show that truncated systems will resonate at wavelengths shorter than their infinite array counterparts, consistent with the behavior observed in Fig. 3 for our structures.

The physical mechanism of a red-shift with increase in coupling between neighboring plasmonic or optical antenna elements is due to a softening of the effective potential for the collective electron motion [61]. In an effort to gain further insight into the physical details of the shift in resonant wavelength with respect to array dimensions, spatial simulations were carried out by discretizing the loop elements and underlying structure, then calculating the spectral absorptivity from volume loss density inside each cell. As before, the structures were simulated with s-polarized excitation at an angle 60 degrees off-normal. These results are shown in Fig. 9, in the form of a spatio-spectral graph, where the wavelength of peak absorptivity is plotted over a schematic drawing of each array. It is again noted that the s-polarized electric field excitation is along the horizontal direction in the Fig. A general trend of a red-shift with increasing array size is seen in agreement with what was observed in the far-field absorptivity plot (Fig. 3) when considering the average peak absorptivity of all the elements within each truncated array. However, the physical relationships causing shifting of peak absorptivity between individual elements are quite complex.

We have observed here as well as in previous experiments and simulations that the wavelength of resonance gradually becomes shorter and converges toward that of a single element as the array dimensionality is reduced, presumably due to the decrease in nearest and second-nearest neighbor coupling as the array dimensions are decreased. For a very large finite array, one would expect the local resonant wavelength to tend toward shorter wavelengths on the edges and toward longer wavelengths in the center. This trend is indeed observed for several of the element rows plotted in Fig. 9; however, it is clear that the mutual coupling in the truncated arrays bears considerable complexity. The 60 degree angle of incidence causes additional modulation in the vertical direction. A gradual shift of resonant

#208167 - $15.00 USD Received 12 Mar 2014; revised 18 Jun 2014; accepted 19 Jun 2014; published 27 Jun 2014

wavelength for each column should be readily observed at the edges of a large (pseudo-infinite) array, which is the topic of another ongoing investigation.

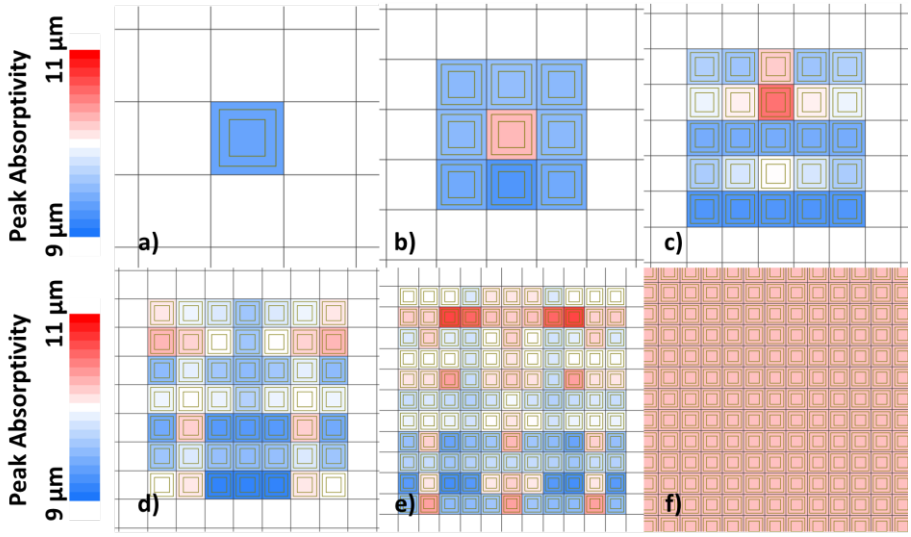

Fig. 9. Simulated peak absorptivity within each cell for a) an isolated loop, b) a 3x3 array, c) a 5x5 array, d) a 7x7 array, e) an 11x11 array, and f) an infinite array.

Despite the wide distribution of peak wavelength shown for the 7x7 and 11x11 arrays in Fig. 9, it is worth noting that the linewidth as shown in Fig. 4 does not increase over that of the infinite array for both the experimental and simulated FWHM values. However, the spatio-spectral graph is slightly misleading since it refers only to the resonant wavelength without showing the corresponding amplitude of the resonance. The experimental and simulated near-field amplitude plots shown in Figs. 5 and 6 in fact indicate stronger amplitude toward the top of the structures, which spatially suggests a greater absorptivity of the wavelength of excitation. Thus, certain unit cells contribute more significantly to the overall absorptivity and the net far-field response corresponds to a weighted average of the emission from the different elements of the array. It is noted that the simulations in Figs. 3 and 9 are the exact same except for the fact that the computational domain was discretized for Fig. 9 such that absorptivity could be calculated within each unit cell. While this process altered the initial mesh of the simulations, the adaptive meshing technique used in Ansys HFSS gave the same result when considering the entire structure in both cases.

Just as related literature is scarce regarding truncation effects in the far-field, there are only a few results which report near-field phenomena, all at RF. Grounds and Well reported simulated results for an infinite by 7 element patch array where the current density is significantly greater on the edge elements at both normal and 30 degree angles of incidence [43]. Contrary to this, Ko and Mittra showed no significant edge effects in the current density with simulated values on an infinite by 9 element wide patch array [32]. Ekpo, Batchelor, and Parker have published the only report which to our knowledge shows near-field mapping of truncated arrays [48]. Here, the transmitted near-field power was mapped over a 3x3 square loop array through its resonance at 400 MHz; the results showed the expected stop-band and pass-band behavior [48]. The near-field results presented in this report show truncation effects in terms of a disruption in the uniformity of the amplitude and phase of the electric field polarized normal to the sample. These results share qualitative agreement with the simulations; although the truncation effects at the edges of the arrays appear more significant than the simulations would predict.

#208167 - $15.00 USD Received 12 Mar 2014; revised 18 Jun 2014; accepted 19 Jun 2014; published 27 Jun 2014

It should be noted that the simulations and measurements described here can be explicitly applied to only the metasurface design which was presented; however, the results should be applicable to a range of element geometries with square symmetry and close inter-element spacing. While there are many combinations of element geometries, sizes, and material system choices within the realm of metasurface design, we believe that our results should provide a baseline result for future researchers concerned with array truncation effects in the infrared and optical regime.

6. Conclusion

Square loop metasurfaces of different array size were designed and fabricated with peak absorptivity at 9.4-10.3 μm at 60 degrees off-normal. Truncation effects were examined for reduced element dimensions 11x11, 7x7, 5x5, 3x3, and isolated square loops using near-field imaging and far-field spectroscopy. The results show the far-field effects of truncation in terms of blue-shifts of the resonant wavelength with decreasing array size. The truncation effects manifest themselves in the near-field in terms of spatial inhomogeneities in the local electric field amplitude and phase distribution. Finite element method simulations show a correspondingly rich spatial distribution of near-field spectral signature at the level of the individual loop elements composing the arrays. The results suggest a complex pattern of mutual coupling, sensitively depending on array size, is responsible for the observed spectral shifts.

Acknowledgments

Funding from the National Science Foundation (NSF CAREER grant CHE 0748226, NSF grant 1204993, and NSF grant 1068050) is gratefully acknowledged. JD wholeheartedly acknowledges support from the SMART Scholarship, funded by OSD-T&E (Office of Secretary Defense-Test and Evaluation), Defense –Wide / PE0601120D8Z National Defense Education Program (NDEP) / BA-1, Basic Research. A portion of the fabrication work was performed by D. Brown and T. Goel at the Georgia Tech Institute for Electronics and Nanotechnology, a member of the National Nanotechnology Infrastructure Network, which is supported by the National Science Foundation. We thank them for their efforts and expertise involving the electron beam lithography. We additionally thank T. Tiwald of J. A. Woollam for helpful suggestions regarding the reflectivity measurements made using the IR ellipsometer and M. Devereaux at Photo Etch Technology for guidance in creating the aperture masks.

#208167 - $15.00 USD Received 12 Mar 2014; revised 18 Jun 2014; accepted 19 Jun 2014; published 27 Jun 2014